



Research Article

Mesoporous Ce-doped Ti:Ash Photocatalyst Investigation in Visible Light Photocatalytic Water Pretreatment Process

Abdulkarim Abdulrahman Mohamed Suliman¹, Ruzinah Isha^{1,*}, Mazrul Nizam Abu Seman¹, Abdul Latif Ahmad², Jamil Roslan¹

¹Faculty of Engineering Technology of Chemical and Process, Universiti Malaysia Pahang, Lebuhraya Tun Razak, 23600 Kuantan Pahang, Malaysia.

²School of Chemical Engineering, Universiti Sains Malaysia, Engineering Campus, 14300 Nibong Tebal, Pulau Pinang, Malaysia.

Received: 10th January 2020; Revised: 3rd April 2020; Accepted: 4th April 2020;
Available online: 30th July 2020; Published regularly: August 2020

Abstract

The treatment of organic pollutants in water including semiconductor photocatalysis is a promising approach to disinfect water. The objective of this study is to investigate the effect of Ce loaded on mesoporous Ti:Ash catalyst for water pretreatment process. The mesoporous Ti:Ash catalyst that doped with Ce was synthesized through wet impregnation method with 5%, 10%, and 15% weight percentage of Ce doped on 40:60 Ti:Ash. The photocatalytic properties were characterized through X-ray powder diffraction, scanning electron microscopy with energy-dispersive X-ray spectroscopy, N₂ adsorption-desorption studies and diffuse reflectance UV-vis absorption spectroscopy. It is found that the Ti:Ash nanocomposites doped with Ce shifted the light absorption band-edge position to the visible region. Moreover, the Ce doped Ti:Ash has large surface area and pore diameter. The Ce doping could significantly improve the absorption edge of visible light and adjust the cut-off absorption wavelength from 404 nm to 451, 477 and 496 nm for 5%, 10% and 15% Ce-doped mesoporous Ti:Ash catalysts, respectively. As the Ce doping ratio increased, the band gaps decreased from 3.06 eV to 2.53 eV. The most contaminant reduction up to 45% was achieved when Ti:Ash:Ce 40:55:5 was used. Higher Ce loading on the photocatalyst may reduce the photocatalyst performance because supernumerary metal loading on TiO₂ can block TiO₂ defect sites which are necessary for the adsorption and photoactivation. The OPFA also acts as an adsorbent for some pollutants besides, reducing the water salinity. It can be deduced that the hybrid TiO₂ photocatalyst that synthesized with OPFA and doped with Ce has huge potential to treat seawater prior to commercial seawater desalination process. Copyright © 2020 BCREC Group. All rights reserved

Keywords: Cerium; Humic acid; Palm oil fiber ash; Photocatalysis; Titanium dioxide; seawater pretreatment

How to Cite: Suliman, A.A.M., Isha, R., Seman, M.N.A., Ahmad, A.L., Roslan, J. (2020). Mesoporous Ce-doped Ti:Ash Photocatalyst Investigation in Visible Light Photocatalytic Water Pretreatment Process. *Bulletin of Chemical Reaction Engineering & Catalysis*, 15(2), 367-378 (doi:10.9767/bcrec.15.2.7055.367-378)

Permalink/DOI: <https://doi.org/10.9767/bcrec.15.2.7055.367-378>

1. Introduction

Palm oil is important agriculture Malaysia commodity. Oil palm fiber ash (OPFA) can be found in the boiler from palm oil production. A poorly managed of OPFA in the boiler may

cause fouling. The OPFA is rich in silica (42%) and the carbon content in the biomass as is about 7.93% [1,2]. Meanwhile, titanium dioxide (TiO₂) shows an excellent degradation rate for organic pollutants in air and water because of its unique properties, such as photostability, low toxicity, availability and reusability [3-5]. Photocatalytic degradation systems using fine TiO₂ powder under UV irradiation have been widely investigated. However, TiO₂ has not yet been

* Corresponding Author.

E-mail: ruzinah@ump.edu.my (R. Isha);
Telp: +6095492891, Fax: +6095492889

successfully used as a commercial catalyst because of limitations of the light wavelength range to activate catalysts [6]. UV that reaches Earth is represented by less than ~4% compared with ~45% of visible light. The fast recombination of a photogenerated hole-electron pair results in a low photocatalytic efficiency with pure titanium [7]. Undesirable electron and hole recombination and low efficiency under irradiation in the visible region are two main drawbacks associated with the use of pure TiO₂ [8-10]. Shifting the light absorption band-edge position to the visible region should be continuously enhanced, and a high photoreaction rate of TiO₂ should be obtained. A TiO₂ photocatalyst that hybrid with oil palm fiber ash (OPFA) used in seawater pre-treatment processes is a new approach in photocatalyst development. The combination of TiO₂ and OPFA alleviates seawater contamination; OPFA acts as an adsorbent of some pollutants and eliminates water salinity where Ti:Ash 40:60 has shown excellent performance in the degradation of humic acid in artificial seawater (ASW) under UV light [1,11]. The surface of TiO₂ and its properties have been extensively modified through doping or co-deposition of metals with TiO₂ by different methods to reinforce photocatalytic activities [12-15].

The introduction of rare-earth metal elements can remarkably enhance photocatalytic efficiency. However, this method is limited due to high costs [16-18]. The photocatalytic activity of TiO₂ can be significantly improved by doping with lanthanide ions/oxides because lanthanide ions can form complexes with various Lewis bases through the interaction of functional groups with their *f*-orbital [19,20]. Amongst lanthanide oxides, Ce exhibits desirable properties as a dopant because it increases oxygen vacancy formation with the high mobility of oxygen species [21]. Liu *et al.* reported that CeO_{2-y}-TiO₂ powders can shift the UV absorption band of TiO₂ to a visible light range [22,23]. Aman *et al.* claimed that the activity of a Ce-TiO₂ photocatalyst depends on the presence of (Ce³⁺/Ce⁴⁺) and the absorption of visible light [24]. In the same context, Makdee *et al.* reported that, doped TiO₂ with cerium improved photocatalytic activity due to the creation of new energy levels by (Ce³⁺/Ce⁴⁺) and oxygen vacancy under the TiO₂ conduction band, which can decrease the charge recombination through trapping the electrons [25]. In synthesized materials, an increasing Ce content shifts light absorption to the visible region and shows a high surface area [6]. Furthermore, excited electrons are trapped by Ce⁴⁺ and transferred

to the adsorbed O₂ molecules to produce superoxide anion radicals [26]. Therefore, doping TiO₂ with Ce introduces a new energy level between valence and conduction bands, leading to a reduction in the band gap of nano TiO₂ and allowing the use of light with a wavelength of over 380 nm (visible light).

This paper presents the effect of OPFA and Ce addition in TiO₂ photocatalyst to treat humic acid contaminated seawater pretreatment. The hybrid photocatalyst was synthesized from Ti:Ash 40:60 with a different mass ratio of Cerium 5%, 10%, and 15% wt., through wet impregnation method, characterized and tested at various times in a 1-L reactor under visible light irradiation. The photocatalysts were characterized by X-ray diffraction (XRD), surface area analysis (BET), Scanning Electron Microscopy (SEM), Energy Dispersive X-Ray Spectroscopy (EDX), and UV-Vis Diffuse Reflectance Spectroscopy.

2. Materials and Methods

2.1 Catalyst Preparations

The materials to prepare Ti:Ash was described in our previous study [9]. The support of the photocatalyst was prepared where the OPFA was calcined at 600 °C, ground and sieved to a particle size less than 125 µm. Then, the Ce-doped TiO₂ materials with different mass percentages of cerium (5, 10, and 15 % (w/w)) were prepared via wet impregnation method. Cerium(III) nitrate hexahydrate (Ce(NO₃)₃·6H₂O) was used as metal cations source. An amount of cerium(III) nitrate and oil palm fiber ash (OPFA) and TiO₂ were prepared at ratio of Ti:Ash:Ce to 40:55:5, 40:50:10, and 40:45:15. Firstly, the desired amount of (Ce(NO₃)₃·6H₂O) was dissolved in 100 mL of distilled water and stirred. Then, TiO₂ and OPFA were gradually added to the solution and stirred for approximately 15 min at 80 °C for 4 h. The slurry mixture was dried in an oven at 120 °C overnight. The dried materials were calcined in a furnace at 500 °C for 4 h. All the prepared solids were ground and sieved to a particle size less than 125 µm. The catalyst was denoted as Ti:Ash:Ce x:y:z, where x, y and z represent the mass ratios of TiO₂, OPFA and Ce, respectively.

2.2 Catalyst Characterization

The microstructure of the doped photocatalyst was characterized using XRD (Rigaku Miniflex II) that equipped with a Cu K α source at a wavelength (λ) of 1.5405 Å at 15 mA, 30

kV and scanned in the 2θ range of 10° – 80° at 4 min^{-1} . The specific surface area ($\text{m}^2\cdot\text{g}^{-1}$), pore size (nm) and total pore volume ($\text{cm}^3\cdot\text{g}^{-1}$) of each photocatalyst were analyzed via N_2 adsorption–desorption by using Micromeritic apparatus in which the catalyst was outgassed at 200°C for 6 h prior to analysis. The absorption spectra of the synthesized materials were determined in the scan range of 200–800 nm by using a UV–vis spectrophotometer (Shimadzu model 2450), and the band gap energies of the prepared catalysts were calculated using a Kubelka–Munk module [24]. The surface morphology of the prepared photocatalysts was characterized through SEM. Meanwhile, the elements analysis was identified through EDX (QUANTA 450).

2.3 Photocatalytic Water Pretreatment Procedure

The sample of contaminated seawater was prepared by dissolving the 1 g of Humic acid in one L of deionized water, followed by addition of 2 pellets of NaOH to prepare a stock solution. Then, 15 ml of stock solution was added to one L of deionized water with 30 g of NaCl. The solution was mixed well with a stirrer to ensure that all salts are dissolved.

A 1 L-capacity borosilicate reactor was used to conduct the photocatalytic reaction on water sample under visible light irradiation (Figure 1). The reactor was covered with aluminium plate to increase light intensity and prevent energy loss from the photoreactor system during the reaction. The reactor was placed in a black box to avoid the interference of external light during the reaction. The reactor was equipped with a visible light 420 nm wavelength lamp.

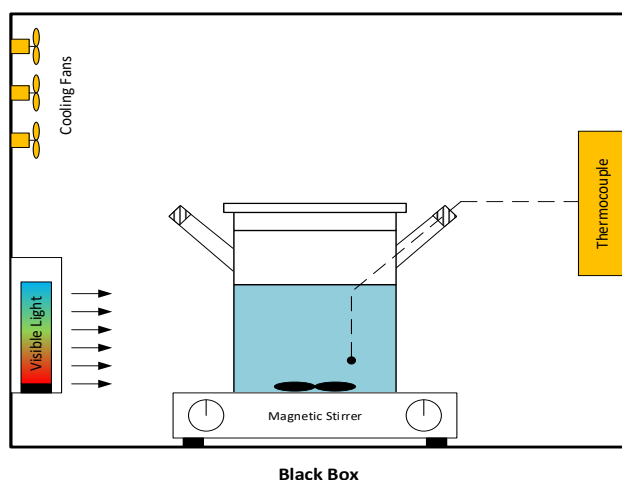


Figure 1. Schematic diagram of the batch photocatalytic reactor set up.

Each run was performed for 1, 2, 3, and 4 h and simultaneously stirred at 300 rpm to ensure the solution was well mixed. The ratio of the photocatalyst to the water sample was 1:300 where approximately 2.7 g of the photocatalyst was added into 800 ml of water sample. After the reaction was conducted, the photocatalyst was filtered from the solution. A COD digestion high-range reagent vial (435 COD HR) was used to determine the organic compound in water sample before and after each run. All the measurements were repeated for three times to ensure data reliability, and the average was obtained.

3. Results and Discussion

3.1 Catalyst Characterization

The XRD patterns of Ti:Ash:Ce 40:60:0, Ti:Ash:Ce 40:55:5, Ti:Ash:Ce 40:50:10 and Ti:Ash:Ce 40:45:15 are presented in Figure 2. The patterns showed the characteristic diffraction peaks at approximately $2\theta = 25.42, 37.24, 37.87, 38.65, 62.28, 62.76$ and 75.11 which could be perfectly indexed to the (101), (103), (004), (112), (213), (204) and (215) crystal faces of the anatase phase of TiO_2 (JCPDS: 9015929), respectively. Same observation of diffraction peaks of anatase was also reported by several researchers [9,18,27]. The crystallite size of the synthesized materials was calculated by using Scherrer's equation from the (101) crystal plane of the anatase phases at 44.8, 50.8, 51.6 and 47.2 nm for Ti:Ash:Ce 40:60:0, Ti:Ash:Ce 40:55:5, 40:50:10 and 40:45:15, respectively. Crystal size increased as the Ce dopant concentration increased from 5% to 10%; however, as the concentration further increased (15%), the particle size decreased to

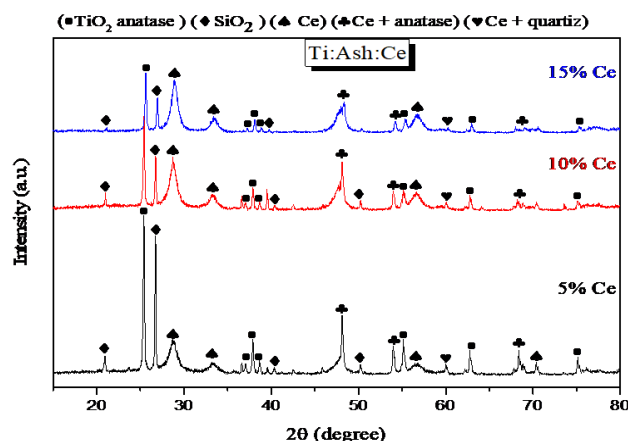


Figure 2. XRD results of synthesized photocatalysts.

42.4 nm. Crystal size decreased as dopant concentration increased because Ce crystals on a TiO₂ lattice surface suppressed the crystallite growth of TiO₂ nanoparticles. Myilsamy *et al.* also claimed that particle size decreases as dopant concentration increases because CeO₂ crystals prevent crystallite growth [20]. The XRD profile of the synthesized materials revealed that Ce species should be in the form of CeO₂ modified on a TiO₂ surface.

This finding may be also due to the high dopant concentration of Ce. Furthermore, the ceria–titania solid solution appeared at approximately $2\theta = 48.20, 54.02,$ and 68.74 . Another solid solution of a ceria–silica peak was shown at approximately $2\theta = 60.11$ with crystal sizes of 65.5, 31.6, and 21.5 nm for 5%, 10%, and 15% of Ce loaded, respectively. Thus, it can be deduced that an increased Ce-doped concentration caused a decrease in the crystal size of the solid solution of ceria–silica. The XRD patterns of ash (OPFA) showed that the characteristic peaks of the crystalline phase at approximately $2\theta = 20.96, 40.38,$ and 50.21 corresponded to quartz.

Figure 3a shows the diffuse reflectance UV–vis absorption spectra of Ti:Ash:Ce. Doping Ce on Ti:Ash could significantly influence the absorption of light and band gap. Figure 3a also reveals that the red shift of the increased doping concentration of Ce was better than that of

a Ti:Ash:Ce 40:60:0 hybrid photocatalyst. The cut-off absorption wavelength was expanded to the visible areas by doping Ce with Ti:Ash.

The band gap energy of the synthesized material was calculated using the Kubelka–Munk function [5,6]. Figure 3b illustrates that band gap energy decreased as the doping ratio increased. It can be seen that Ti:Ash:Ce 40:60:0, Ti:Ash:Ce 40:55:5, 40:50:10 and 40:45:15 had onsets of absorbance of 3.06, 2.72, 2.61 and 2.53 eV, respectively. As the doping ratio increased from 0% to 15%, the cut-off wavelength expanded from 404 nm to 496 nm. Thus, the band gap decreased from 3.06 eV to 2.53 eV.

The cut-off wavelength and the band gap energy of each sample are tabulated in Table 1. The result confirmed that doping Ce with Ti:Ash 40:60 could reduce the wideness of the forbidden band of TiO₂ nanomaterials. The band gap decreased because the doped Ce ions in TiO₂ nanopowders cause lattice distortion and introduce impurity to the forbidden band of TiO₂ [6,28]. Whereas, the electron can transfer in the valence band or conduction band between the doping and raw materials [29,30]. Tong *et al.* reported that the energy of the conduction band in TiO₂ is larger than that of the 4f orbital energy level of Ce; thus, the 4f orbital of Ce plays a crucial role in generating charge carries (e⁻, h⁺) under visible irradiation [31,32].

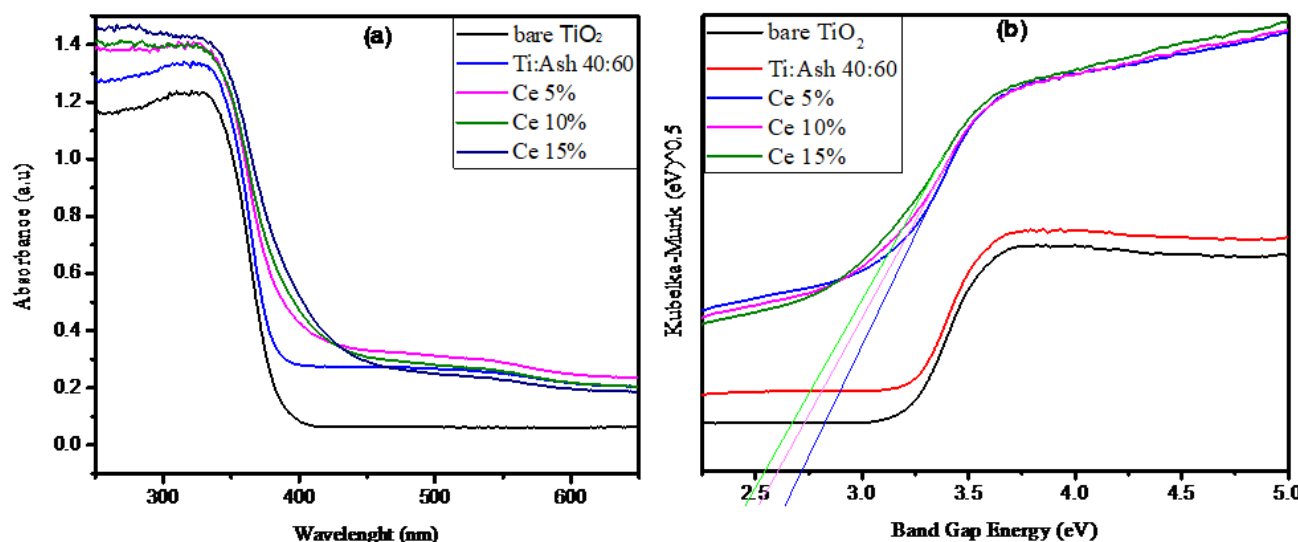


Figure 3. (a) Results obtained from UV-Vis DRS. (b) Kubelka-Munk plot for band gap.

Table 1. Cut-off wavelength and band gap of Ti:Ash 40:60 doped with different ratio of Ce.

Samples	Ti:Ash 40:60	Ti:Ash:Ce 40:55:5	Ti:Ash:Ce 40:50:10	Ti:Ash:Ce 40:45:15
Cut-off wavelength (nm)	404	451	477	496
Band gap (eV)	3.06	2.72	2.61	2.53

The pore structure and specific surface areas of all the samples were investigated on the basis of N₂ adsorption–desorption isotherm. As shown in Figure 4, these samples showed type IV isotherms, indicating the mesoporous structure of the samples. The corresponding hysteresis loops were type H₃ at a high relative pressure range between 0.65 and 1.0 for Ti:Ash:Ce 40:55:5 and Ti:Ash:Ce 40:50:10. The relative pressure range of Ti:Ash:Ce 40:55:15 was from 0.2 to 1, suggesting that Ti:Ash:Ce 40:55:15 could be an effective absorbent. The appear-

ance of hysteresis loops supports the presence of slit-like pores [16,19].

Table 2 presents the results of BET analysis to determine the surface area, pore volume and pore size of the fresh and spent of Ti:Ash:Ce photocatalyst. The BET surface area of Ti:Ash:Ce 40:60:0 increased from 3.9 m².g⁻¹ to 6.1 m².g⁻¹ after the reaction. The same pattern of increment was observed in Ti:Ash:Ce 40:55:5 and 40:55:10 photocatalyst as the photocatalyst surface area rose from 11.54 m².g⁻¹ to 18.21 m².g⁻¹ and from 10.43 m².g⁻¹ to 18.06 m².g⁻¹,

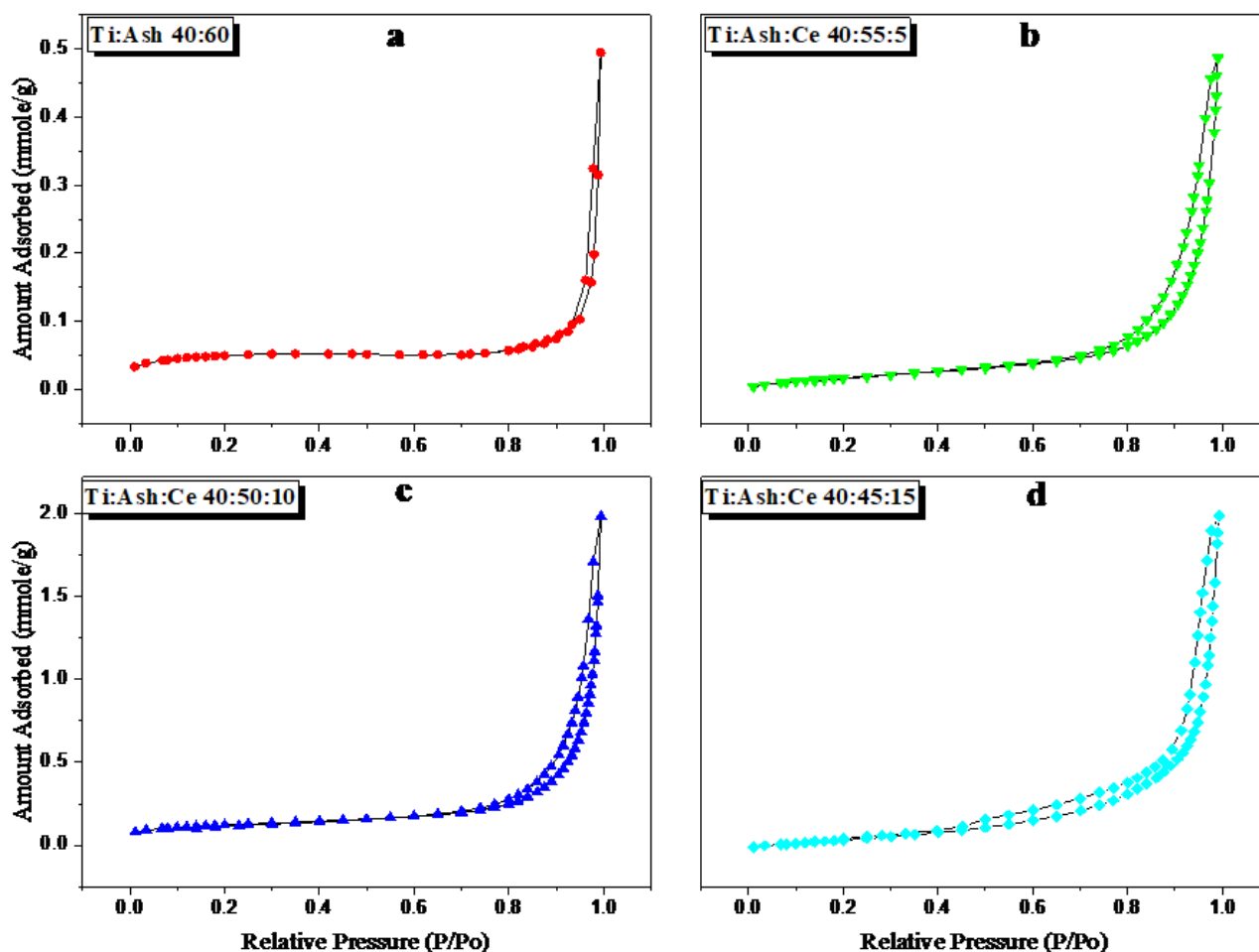


Figure 4. BET adsorption isotherms for the Ce-doped samples, (a) Ti:Ash 40:60, (b) Ti:Ash:Ce 40:55:5, (c) Ti:Ash:Ce 40:50:10, and (d) Ti:Ash:Ce 40:45:15.

Table 2. The microstructure analysis of hybrid Ti:Ash:Ce photocatalysts.

Ce loading (%)	Specific surface area (m ² .g ⁻¹)		Pore volume × 10 ² (cm ³ .g ⁻¹)		Pore size (nm)	
	Before	After	Before	After	Before	After
0% Ce	3.90	6.10	7.10	3.20	21.50	17.40
5% Ce	11.54	18.21	3.04	3.51	10.55	7.78
10% Ce	10.43	18.06	4.50	4.17	1549.	9.17
15% Ce	11.60	19.54	6.03	6.03	20.80	12.35

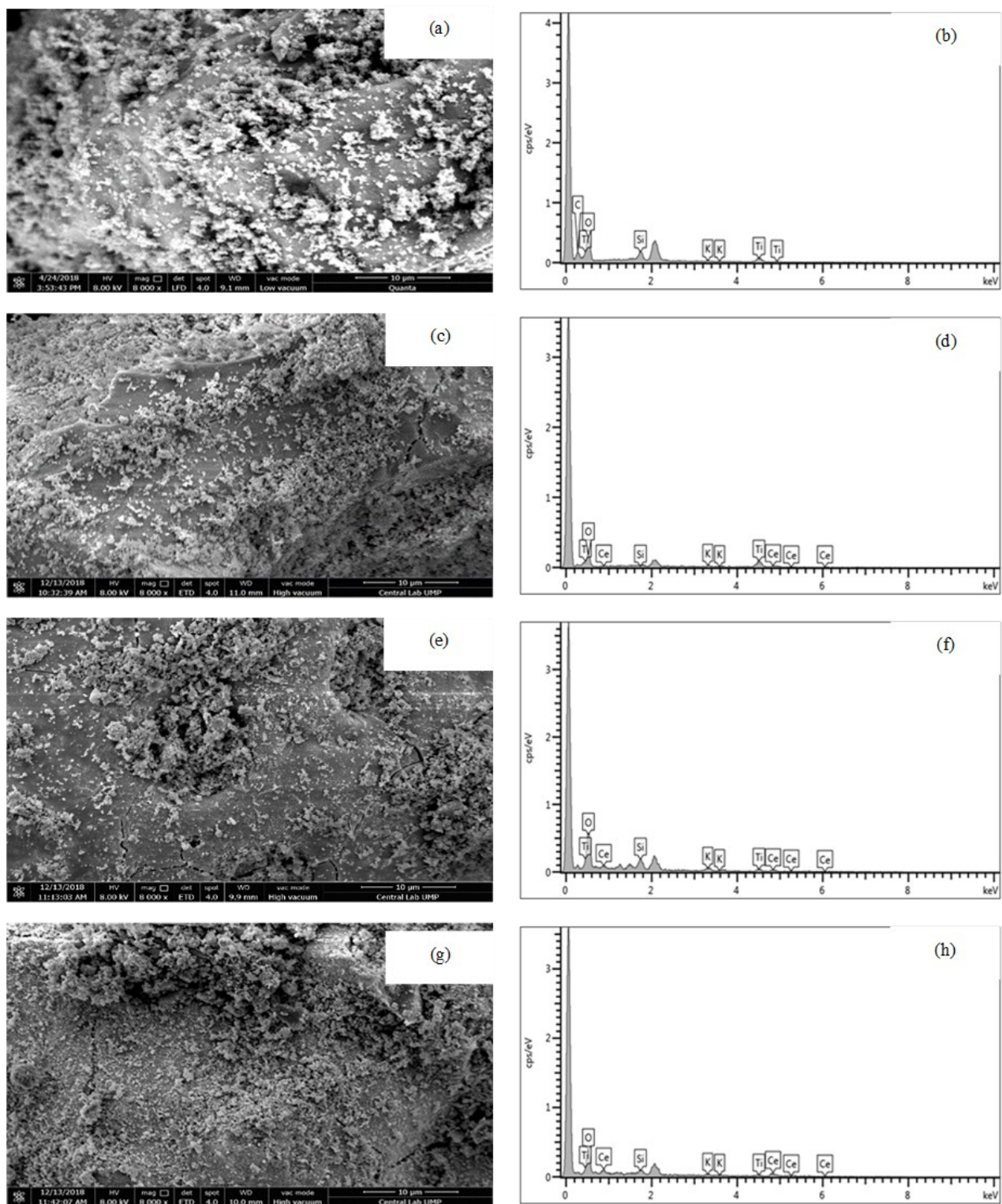


Figure 5. SEM and EDX images of catalysts with 8000X magnification: a) the SEM of fresh Ti:ash 40:60, b) EDX of Ti:ash 40:60, c) SEM of fresh Ti:Ash:Ce 40:55:5, d) EDX of Ti:Ash:Ce 40:55:5, e) SEM of fresh Ti:Ash:Ce 40:50:10, f) EDX of Ti:Ash:Ce 40:50:10, g) SEM of fresh Ti:Ash:Ce 40:45:15, h) EDX of Ti:Ash:Ce 40:45:15.

respectively. The surface area of Ti:Ash:Ce 40:55:15 also increased from 11.60 m².g⁻¹ to 19.54 m².g⁻¹.

The morphological characteristics and phase composition of the photocatalysts were analyzed through SEM and EDX. Whereas, the TiO₂ and OPFA were investigated in our previous study [9]. Figure 5a presents the SEM image of the Ti:Ash:Ce 40:60:0, that is, the well-dispersed tiny spherical aggregated particles with different diameters. Figures. 5c, 5e, and 5g illustrate the images of the as-synthesized samples of Ti:Ash:Ce 40:55:5, 40:50:10 and 40:45:15, respectively. The SEM image of the prepared samples shows the inbuilt mesopore structure in the aggregated particles. Agglomeration was affected by increasing the amount of Ce. Myilsamy *et al.* similarly reported that the tendency of individual particles of TiO₂ to agglomerate is affected by the presence of (Ce⁴⁺/Ce³⁺) and spherical aggregates of particles with varying sizes and large irregular voids distributed amongst the particles [20]. The images also display a well-dispersed of TiO₂ and Ce on the OPFA surface in all the synthesized photocatalysts. This finding indicated that thorough mixing enhanced the dispersion of TiO₂ ash and Ce during catalyst preparation. The EDX spectrum of Ti:Ash:Ce 40:60:0 is shown in Figure 5b. The other photocatalyst sample is illustrated in Figures 5d, 5f and 5h. The Ti, O, Si and Ce peaks were found in the spectra, confirming the presence Ce in TiO₂ nanoparticles.

3.2 Photocatalytic Degradation of Humic Acid

Prior to this investigation, when visible light was exposed to the water sample alone, no significant change of water COD and salinity

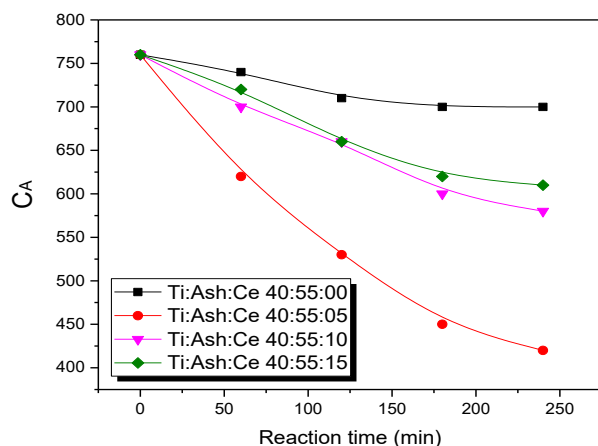


Figure 6. COD profiles of treated water using photocatalysts.

were obtained. The Ti:Ash:Ce 40:60:0 was then tested without light irradiation for 240 minutes. It is found that no significant change of COD was observed but a slight decrease of water salinity was observed. This indicates that adsorption of contaminant did not occur.

Figure 6 shows the COD profiles of water samples tested after 240 min in visible light irradiation. The Ti:Ash:Ce 40:60:0 was tested under visible light to serve as a blank run, no significant change was found. This was because the band gap energy of Ti:Ash:Ce 40:60:0 is 3.06 eV which reactive in UV light. The slight reduction of COD in the first 100 minutes might be caused by the adsorption of contaminants by ash. Oil palm fiber ash (OPFA) has been used as a low-cost substitute adsorbent to eliminate harmful coloration such as malachite green (MG), methylene blue, an anionic dye, direct blue 71 [33-35]. The Langmuir balance isotherm is more accurate than the other isotherm equations to explain the adsorption in the oil-palm shell of aqueous phenol [36,37]. The investigation was done by Kan *et al.* indicate that the silica content in OPFA might enhance the adsorption ability of photocatalyst in seawater pretreatment [11]. Silica content in OPFA might enhance the catalyst uses in seawater pretreatment by improving adsorbing characteristic. Moreover, appearance salt peaks on spent catalysts support this observation.

Humic acids (HA) constitute a vast majority of natural organic matter (NOM) and are commonly present in natural water and strictly affect its taste and color [38,39]. Humic acids are compounds distinguished by high levels of carboxyl (-COOH) and phenolic hydroxyl (-OH) groups bound to aromatic chains. Since they are a very complex mixture, they cannot be represented by a simple formula [40,41]. Humic acid comes from the soil, river, and lake sediments, coral, freshwater, wastewaters, plants and coral skeletons [42]. One of the sources of HA in seawater is aquaculture, This can be done by the addition of humic acid in the formula of the feed, which can lower the accumulation of heavy metals in the fish body [43,44]. Humic acids is among the common contaminants that can be found in water source. Humic acid can be degraded into free radicals, such as singlet oxygen, humic-derived peroxy radicals by solvated electron and OH[•] radicals [4]. The presence of different transition metal oxides, such as: TiO₂, CuO, Fe₂O₃ and ZnO, in OPFA promotes environmentally persistent free radicals in the form of metal

cations or redox potentials of metal ions [10,45] for contaminants degradations.

As can be seen in Figure 6, a significant decreasing trend of COD reduction was observed when Ti:Ash:Ce 40:55:5 was used. Generally, it was found that a reduction of 18% of contaminants was observed after tested for 60 min, while 30%, 41%, and 45% was observed after testing for 120 min, 180 min, and 240 min respectively. In contrast, the COD profiles for Ti:Ash:Ce 40:50:10 and Ti:Ash:Ce 40:45:15 photocatalysts showed less activity than Ti:Ash:Ce 40:55:5. When Ti:Ash:Ce 40:50:10 was used, 8%, 13%, 21%, and 24% of COD reduction was obtained after testing for 60 min, 120 min, 180 min, and 240 min. respectively. Meanwhile, a reduction of 5%, 13%, 18%, and 20% was obtained when Ti:Ash:Ce 40:45:15 was used after 60 min, 120 min, 180 min, and 240 min, respectively.

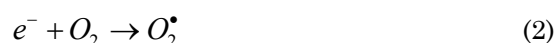
The highest contaminants reduction was achieved when Ti:Ash:Ce 40:55:5 was used. It might be caused by the Ti:Ash:Ce 40:55:5 photocatalyst band gap energy of 2.72 eV, which reactive in visible light. Moreover, excellent Ce metal distribution on the photocatalyst surface and textural properties might contribute to remarkable performance of Ti:Ash:Ce 40:55:5. The optimum metal loading in the photocatalyst is also important because suitable amount of metal loading enhances the photoactivity of catalysts by increasing the number of electron trapping sites [14,46]. In addition, the amount of metal loading is crucial because supernumerary metal loading on TiO₂ can block TiO₂ defect sites which are necessary for the adsorption and photoactivation of oxygen, thereby reduc-

ing the photoactivity of organic degradation [47,48].

3.3 Possible Catalytic Mechanism

Numerous studies have been conducted to identify the catalytic mechanism and the reactive species responsible for organic compound degradation. The essential reactive species are electrons (e⁻), holes (h⁺) and hydroxyl free radicals (OH[•]). Thus, Ce 4f level in Ti:Ash:Ce plays a vital role in interfacial charge transfer and restraint of electron-hole recombination. Besides that, The combined interaction between Ti and Ce metal cations promotes an easy charge transfer on surfaces, accelerating the Ce³⁺ redox process that is beneficial to oxidation [7,49]. Makdee *et al.* reported that doped TiO₂ with cerium improved photocatalytic activity due to the creation of new energy levels by Ce³⁺ and oxygen vacancy under the TiO₂ conduction band, which can decrease the charge recombination through trapping the electrons [25]. Moreover, cerium ions could form complexes with various Lewis bases in the interaction of the functional groups with their f-orbital, which promote the photocatalytic activity either by the presence of redox couple or different optical properties caused by different ions, Ce³⁺ [20,50].

On the other hand, oxygen has an ability to accept and consume the generated electrons in the photo-degradation reaction and producing free radical species through the following steps:



After producing the superoxide free radicals (O₂[•]), the second stage of photo-degradation will start to produce the reactive free radical species (hydroxyl radical OH[•]). The process of generating OH[•] can occur by two pathways; first O₂ present in water is reduced to form O₂[•], which then reacts with H⁺ to form OOH[•], followed by rapid decomposition to OH[•]. The second pathway involves the oxidation of 2H⁺,

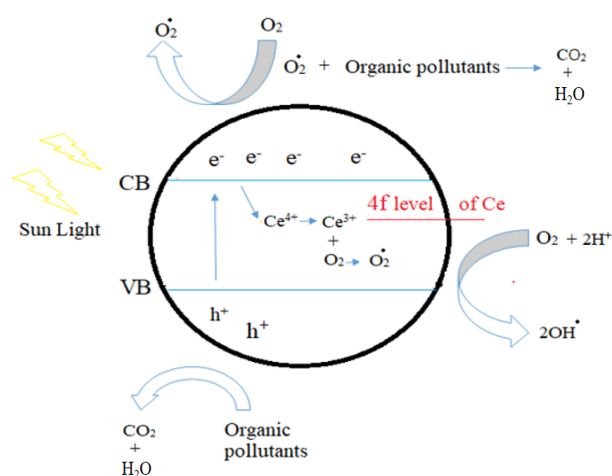


Figure 7. Schematic photocatalysis mechanism of Ti:Ash:Ce photocatalysts.

Table 3. The *k*-value for each set of photoreaction with their corresponding R²-value.

Photocatalyst	<i>k</i> (min ⁻¹)	R ²
Ti:Ash:Ce 40:55:05	0.0025	0.9764
Ti:Ash:Ce 40:50:10	0.0012	0.9845
Ti:Ash:Ce 40:45:15	0.0010	0.9623

which aid in the decay of contaminants, as shown in Figure 7 [20,22,51].



Furthermore, the kinetics data for different catalyst Ti:Ash:Ce loadings were determined by using Langmuir–Hinshelwood (LH) rate law model. After fitting data on first order reaction, a typical irreversible reaction in this study can be described by the following equation:

$$-r_{COD} = \frac{1}{C_A} = kt + \frac{1}{C_{A0}} \quad (5)$$

where $-r_{COD}$ is COD degradation rate ($\text{mg.L}^{-1}.\text{min}^{-1}$) and the k is a specific reaction time (min^{-1}). The values of the specific reaction time k , and R^2 summarized in Table 3.

4. Conclusions

The activity of TiO_2 for humic acid degradation in water was investigated using photocatalysts of Ti:Ash:Ce which were synthesized at the various mass ratio. The XRD pattern indicates that the crystalline phase of the TiO_2 matrix was stable, and new solid solution peaks were achieved after impregnated with Ce and ash. Furthermore, UV–vis absorption spectroscopy confirmed that Ce loading reduced the energy band gap of photocatalysts from 3.06 eV (Ti:Ash:Ce 40:60:0) to 2.53 eV (Ti:Ash:Ce 40:60:15) which reactive in visible light. The Ce was well dispersed on the Ti:Ash photocatalyst. It is also found that aggregation and agglomeration of the loaded metal increased when the amount of Ce loading increased. The synthesized photocatalyst exhibited type IV isotherms, indicating the mesoporous structure of the photocatalyst. The Ti:Ash:Ce 40:60:0 exhibited a low activity under visible light irradiation while Ti:Ash:Ce 40:55:5 performed the best with up to 45% contaminant reduction was achieved. The higher Ce loading on the photocatalyst may reduce the photocatalyst performance because supernumerary metal loading on TiO_2 can block TiO_2 defect sites which are necessary for the adsorption and photoactivation. It can be deduced that the hybrid TiO_2 photocatalyst that synthesized with OPFA and doped with Ce has huge potential to treat seawater.

Acknowledgment

The authors acknowledge the support of the Universiti Malaysia Pahang (UMP) [RDU1703242 & PGRS160331] and Ministry of Education, and Bright Star University of Tech-

nology, Libya for a PhD scholarship for one of the authors (Abdulkarim Suliman).

References

- [1] Ahmad, T., Danish, M., Rafatullah, M., Ghazali, A., Sulaiman, O., Hashim, R. (2012). The use of date palm as a potential adsorbent for wastewater treatment: a review. *Environmental Science and Pollution Research*, 19, 1464-1484. DOI: 10.1007/s11356-011-0709-8
- [2] Abdullah, N., Sulaiman, F. (2013). The oil palm wastes in Malaysia, in *Biomass Now-Sustainable Growth and Use*, ed: InTech.
- [3] Aman, N., Mishra, T., Sahu, R.K., Tiwari, J.P. (2010). Facile synthesis of mesoporous N doped zirconium titanium mixed oxide nanomaterial with enhanced photocatalytic activity under visible light. *Journal of Materials Chemistry*, 20, 10876-10882. DOI: 10.1039/C0JM01342K
- [4] Andayani, W., Bagyo, A.N. (2011). TiO_2 bead for photocatalytic degradation of humic acid in peat water R. *Indonesian Journal of Chemistry*, 11, 253-257.
- [5] Chen, C., Ma, W., Zhao, J. (2010). Semiconductor-mediated photodegradation of pollutants under visible-light irradiation. *Chemical Society Reviews*, 39, 4206-4219. DOI: 10.1039/B921692H
- [6] Cheng, Y., Zhang, M., Yao, G., Yang, L., Tao, J., Gong, Z. (2016). Band gap manipulation of cerium doping TiO_2 nanopowders by hydrothermal method. *Journal of Alloys and Compounds*, 662, 179-184. DOI: 10.1016/j.jallcom.2015.12.034
- [7] Fiorenza, R., Bellardita, M., Barakat, T., Scirè, S., Palmisano, L. (2018). Visible light photocatalytic activity of macro-mesoporous TiO_2 - CeO_2 inverse opals. *Journal of Photochemistry and Photobiology A: Chemistry*, 352, 25-34. DOI: 10.1016/j.jphotochem.2017.10.052
- [8] Ibhaddon, A.O., Fitzpatrick, P. (2013). Heterogeneous photocatalysis: recent advances and applications. *Catalysts*, 3, 189-218. DOI: 10.3390/catal3010189
- [9] Isha, R., Roslan, J., Suliman, A. (2018). Effect of mass ratio of titanium dioxide and oil palm fiber ash (TiO_2 :Ash) in hybrid photocatalyst on photocatalytic seawater pretreatment. In: *Proceedings of The National Conference for Postgraduate Research (NCON-PGR 2018)*, 124-132.
- [10] Jia, H., Zhao, S., Shi, Y., Zhu, L., Wang, C., Sharma, V.K. (2018). Transformation of polycyclic aromatic hydrocarbons and formation of environmentally persistent free radicals on modified montmorillonite: the role of surface

- metal ions and polycyclic aromatic hydrocarbon molecular properties. *Environmental Science & Technology*, 52, 5725-5733. DOI: 10.1021/acs.est.8b00425
- [11] Kan, W.E., Isha, R. (2016). The effect of light wavelength on water quality in photocatalytic seawater pre-treatment. *In: Proceedings of The National Conference for Postgraduate Research (NCON-PGR 2016)*. 89-94.
- [12] Kan, W.E., Roslan, J., Isha, R. (2016). Effect of Calcination temperature on performance of photocatalytic reactor system for seawater pretreatment. *Bulletin of Chemical Reaction Engineering & Catalysis*, 11(2), 230-237. DOI: 10.9767/brec.11.2.554.230-237
- [13] Khan, M.M., Ansari, S.A., Pradhan, D., Ansari, M.O., Lee, J., Cho, M.H. (2014). Band gap engineered TiO₂ nanoparticles for visible light induced photoelectrochemical and photocatalytic studies. *Journal of Materials Chemistry A*, 2, 637-644. DOI: 10.1039/C3TA14052K
- [14] Khan, M.R., Chuan, T.W., Yousuf, A., Chowdhury, M., Cheng, C.K. (2015). Schottky barrier and surface plasmonic resonance phenomena towards the photocatalytic reaction: study of their mechanisms to enhance photocatalytic activity. *Catalysis Science & Technology*, 5, 2522-2531. DOI: 10.1039/C4CY01545B
- [15] Kharel, P.L., Cuillier, P.M., Fernando, K., Zamborini, F.P., Alphenaar, B.W. (2018). Effect of Rare-Earth Metal Oxide Nanoparticles on the Conductivity of Nanocrystalline Titanium Dioxide: An Electrical and Electrochemical Approach. *The Journal of Physical Chemistry C*, 122, 15090-15096. DOI: 10.1021/acs.jpcc.8b02971
- [16] Liu, J., Li, H., Li, Q., Wang, X., Zhang, M., Yang, J. (2014). Preparation of cerium modified titanium dioxide nanoparticles and investigation of their visible light photocatalytic performance. *International Journal of Photoenergy*, 2014, 9. DOI: 10.1155/2014/695679
- [17] Liu, L., Ji, Z., Zou, W., Gu, X., Deng, Y., Gao, F. (2013). In situ loading transition metal oxide clusters on TiO₂ nanosheets as cocatalysts for exceptional high photoactivity. *Acs Catalysis*, 3, 2052-2061. DOI: 10.1021/cs4002755
- [18] Matějová, L., Kočí, K., Reli, M., Čapek, L., Hospodková, A., Peikertová, P. (2014). Preparation, characterization and photocatalytic properties of cerium doped TiO₂: On the effect of Ce loading on the photocatalytic reduction of carbon dioxide. *Applied Catalysis B: Environmental*, 152, 172-183. DOI: 10.1016/j.apcatb.2014.01.015
- [19] Liu, Z., Guo, B., Hong, L., Jiang, H. (2005). Preparation and characterization of cerium oxide doped TiO₂ nanoparticles. *Journal of Physics and Chemistry of Solids*, 66, 161-167. DOI: 10.1016/j.jpcs.2004.09.002
- [20] Myilsamy, M., Murugesan, V., Mahalakshmi, M. (2015). Indium and cerium co-doped mesoporous TiO₂ nanocomposites with enhanced visible light photocatalytic activity. *Applied Catalysis A: General*, 492, 212-222. DOI: 10.1016/j.apcata.2014.12.035
- [21] Ndinda, E., Park, H., Kim, K.N. (2014). Preparation and characterization of cerium doped titanium dioxide nano powder for photocatalyst. *Korean Journal of Materials Research*, 24, 33-36. DOI: 10.3740/MRSK.2014.24.1.33
- [22] Ng, K.H., Lee, C.H., Khan, M.R., Cheng, C.K. (2016). Photocatalytic degradation of recalcitrant POME waste by using silver doped titania: Photokinetics and scavenging studies. *Chemical Engineering*, 286, 282-290. DOI: 10.1016/j.cej.2015.10.072
- [23] Niu, B., Wang, X., Wu, K., He, X., Zhang, R. (2018). Mesoporous Titanium Dioxide: Synthesis and Applications in Photocatalysis, Energy and Biology. *Materials*, 11, 1910. DOI: 10.3390/ma11101910
- [24] Aman, N., Satapathy, P., Mishra, T., Mahato, M., Das, N. (2012). Synthesis and photocatalytic activity of mesoporous cerium doped TiO₂ as visible light sensitive photocatalyst. *Materials Research Bulletin*, 47, 179-183.
- [25] Makdee, A., Unwiset, P., Chanapatttharapol, K.C., Kidkhunthod, P. (2018). Effects of Ce addition on the properties and photocatalytic activity of TiO₂, investigated by X-ray absorption spectroscopy, *Materials Chemistry and Physics*, 213, 431-443.
- [26] Devi, L.G., Anitha, B. (2019). Effective band gap engineering by the incorporation of Ce, N and S dopant ions into the SrTiO₃ lattice: exploration of photocatalytic activity under UV/solar light. *Journal of Sol-Gel Science and Technology*, 94, 50-66. DOI: 10.1007/s10971-019-05074-4.
- [27] Zheng, R.R., Li, T.T., Yu, H. (2008) Construction of Indium and Cerium Codoped Ordered Mesoporous TiO₂ Aerogel Composite Material and Its High Photocatalytic Activity. *Global Challenges*, 2, 700118.
- [28] Poullos, I., Micropoulou, E., Panou, R., Kostopoulou, E. (2003). Photooxidation of eosin Y in the presence of semiconducting oxides. *Applied Catalysis B: Environmental*, 41, 345-355. DOI:10.1016/S0926-3373(02)00160-1
- [29] Xu, A.W., Gao, Y., Liu, H.Q. (2002). The preparation, characterization, and their photocatalytic activities of rare-earth-doped TiO₂

- nanoparticles. *Journal of Catalysis*, 207, 151-157. DOI: 10.1006/jcat.2002.3539
- [30] Zhu, L., Jo, S.B., Ye, S., Ullah, K., Oh, W.C. (2014). Fabrication of ZnO and TiO₂ Combined Activated Carbon Nanocomposite and Adsorption Enhanced Synergetic Photocatalytic Effects. *Asian Journal of Chemistry*, 26, 1829-1832. DOI: 10.14233/ajchem.2014.15562
- [31] Tong, T., Zhang, J., Tian, B., Chen, F., He, D., Anpo, M. (2007). Preparation of Ce-TiO₂ catalysts by controlled hydrolysis of titanium alkoxide based on esterification reaction and study on its photocatalytic activity. *Journal of colloid and interface science*, 315, 382-388. DOI: 10.1016/j.jcis.2007.06.051
- [32] Polliotto, V., Albanese, E., Livraghi, S., Agnoli, S., Pacchioni, G., Giamello, E. (2018). Structural, electronic and photochemical properties of cerium-doped zirconium titanate. *Catalysis Today*, 340, 49-57. DOI: 10.1016/j.cattod.2018.09.026
- [33] Tan, I., Ahmad, A., Hameed, B. (2008). Adsorption of basic dye using activated carbon prepared from oil palm shell: batch and fixed bed studies. *Desalination*, 225, 13-28.
- [34] Hameed, B., El-Khaiary, M. (2008). Batch removal of malachite green from aqueous solutions by adsorption on oil palm trunk fibre: equilibrium isotherms and kinetic studies. *Journal of Hazardous Materials*, 154 (1-3), 237-244. DOI: 10.1016/j.jhazmat.2007.10.017.
- [35] Ahmad, T., Rafatullah, M., Ghazali, A., Sulaiman, O., Hashim, R. (2011) Oil palm biomass-Based adsorbents for the removal of water pollutants - A review. *Journal of Environmental Science and Health, Part C*, 177-222.
- [36] Adebisi, G.A., Chowdhury, Z.Z., Alaba, P.A. (2017). Equilibrium, kinetic, and thermodynamic studies of lead ion and zinc ion adsorption from aqueous solution onto activated carbon prepared from palm oil mill effluent. *Journal of Cleaner Production*, 148, 958-968. DOI: 10.1016/j.jclepro.2017.02.047.
- [37] Jia, Q., Lua, A.C. (2008). Concentration-dependent branched pore kinetic model for aqueous phase adsorption. *Chemical Engineering Journal*, 136, 227-235.
- [38] Patsios, S., Sarasidis, V., Karabelas, A. (2013). A hybrid photocatalysis-ultrafiltration continuous process for humic acids degradation. *Separation and Purification Technology*, 104, 333-341, DOI: 10.1016/j.seppur.2012.11.033.
- [39] Yusof, M.A.M., Seman, M.N.A., Nizam, M. (2016). Polyamide Forward Osmosis Membrane: Synthesis, Characterization and Its Performance for Humic Acid Removal. *Journal of Membrane Science and Research*, 2 (2), 90-94. DOI: 10.22079/JMSR.2016.19156.
- [40] Haysahi, K.i., Shibata, H., Yui, M., Ohmoto, H. (2001). Experimental Study Assessing the Role of Sedimentary Organic Materials to Control the Redox State of Ground Materials to Control the Redox State of Groundwater: Consumption of Dissolved Oxygen by Humic Acid. *Resource Geology*, 51 (1), 45-54. DOI: 10.1111/j.1751-3928.2001.tb00080.x.
- [41] Szymański, K., Morawski, A.W., Mozia, S. (2016). Humic acids removal in a photocatalytic membrane reactor with a ceramic UF membrane. *Chemical Engineering Journal*, 305, 19-27. DOI: 10.1016/j.cej.2015.10.024.
- [42] Al-Faiyz, Y.S. (2017). CPMA 13C NMR characterization of humic acids from composted agricultural Saudi waste. *Arabian Journal of Chemistry*, 10, S839-S853. DOI: 10.1016/j.arabjc.2012.12.018.
- [43] Wang, W.X., Onsanit, S., Dang, F. (2012). Dietary bioavailability of cadmium, inorganic mercury, and zinc to a marine fish: Effects of food composition and type. *Aquaculture*, 356-357, 98-104. DOI: 10.1016/j.aquaculture.2012.05.031.
- [44] Rasidi, R., Jusadi, D., Setiawati, M., Yuhana, M., Zairin, Jr.M., Sugama, K. (2019). Response to Humic Acid Addition Into Feeds with Heavy Metal Content Made of Green Mussels on Growth of Asian Seabass. *Biotropia*, 26(3). DOI: 10.11598/btb.2019.26.3.1114.
- [45] Yang, L., Liu, G., Zheng, M., Jin, R., Zhao, Y., Wu, X. (2017). Pivotal roles of metal oxides in the formation of environmentally persistent free radicals. *Environmental Science & Technology*, 51, 12329-12336.
- [46] Shan, Z., Wu, J., Xu, F., Huang, F.Q., Ding, H. (2008). Highly effective silver/semiconductor photocatalytic composites prepared by a silver mirror reaction. *The Journal of Physical Chemistry C*, 112, 15423-15428. DOI: 10.1021/jp804482k
- [47] Tian, Y., Tatsuma, T. (2005). Mechanisms and applications of plasmon-induced charge separation at TiO₂ films loaded with gold nanoparticles. *Journal of the American Chemical Society*, 127, 7632-7637. DOI: 10.1021/ja042192u
- [48] Pang, Y.L., Abdullah, A.Z. (2013). Effect of carbon and nitrogen co-doping on characteristics and sonocatalytic activity of TiO₂ nanotubes catalyst for degradation of Rhodamine B in water. *Chemical Engineering Journal*, 214, 129-138. DOI: 10.1016/j.cej.2012.10.036.
- [49] Shi, Z.L., Du, C., Yao, S.H. (2011). Preparation and photocatalytic activity of cerium

- doped anatase titanium dioxide coated magnetite composite. *Journal of the Taiwan Institute of Chemical Engineers*, 42, 652-657. DOI: 10.1016/j.jtice.2010.10.001
- [50] Silva, A.M., Silva, C.G., Dražić, G., Faria, J.L. (2009). Ce-doped TiO₂ for photocatalytic degradation of chlorophenol. *Catalysis Today*, 144, 13-18. DOI: 10.1016/j.cattod.2009.02.022
- [51] Tbessi, I., Benito, M., Molins, E., Llorca, J., Touati, A., Sayadi, S. (2019). Effect of Ce and Mn co-doping on photocatalytic performance of sol-gel TiO₂. *Solid State Sciences*, 88, 20-28. DOI: 10.1016/j.solidstatesciences.2018.12.004